



# Investigation of microstructure, mechanical, and corrosion behavior of nickel-based alloy 625/duplex stainless steel UNS S32205 dissimilar weldments using ERNiCrMo-3 filler metal

M. Tümer<sup>1</sup> · T. Mert<sup>2</sup> · Tuba Karahan<sup>3</sup>

Received: 2 April 2020 / Accepted: 9 October 2020 / Published online: 15 October 2020  
© International Institute of Welding 2020

## Abstract

In this study, nickel-based alloy 625 and duplex stainless steel (DSS) UNS S32205 (2205) dissimilar pairs were welded with metal inert gas (MIG) welding process. Weld metal, obtained with the utilization of ERNiCrMo-3 filler wire, was subjected to mechanical, microstructural, and corrosion investigations. V-notch impact tests and micro hardness measurements were realized on dissimilar weld metal. Microstructural changes in weld metal, fusion line, and heat-affected zone were examined using optical, scanning (SEM), and transmission electron microscopes (TEM) with energy-dispersive spectrometry (EDS). Phase precipitations rich of Nb and Mo were detected among dendritic austenite arms in the weld metal. It was observed that ERNiCrMo-3 filler metal had sufficient toughness because of high nickel content. Corrosion tests revealed that weld metal face pass is the least corrosion-resistant zone in weld metal unlike weld root. This is mainly because more intense intermetallics formed in weld metal face compared with the middle of the weld and the root.

**Keywords** Nickel alloy · Duplex stainless steel · MIG welding · ERNiCrMo-3 wire · Microstructural characterization · Corrosion

## 1 Introduction

Dissimilar joining of nickel-based super alloys and stainless steels are widely used in oil refinery steam generators, chemical tankers, pressure vessels, pipes of heat exchangers, and petrochemical and nuclear energy plants [1, 2]. The most important characteristics of these alloys are their high corrosion resistance in aggressive environment and the ability to fulfill strength requirements at the same time [3–5]. The application

areas of dissimilar joining of Ni-based super alloys and duplex stainless steels are maritime and chemical industry and, in addition, geothermal industry because of their ease of joining, good corrosion resistance, and high strength [6]. Ni-based super alloy loses 1/3 of its yield strength when temperature rises to 485 °C, compared with its strength at 100 °C. Yet, it retains this strength until 820 °C and, even at 700 °C, an increase in strength can be observed and the decrease in yield strength compared with 100 °C would be limited to 25% [7]. Alloy 625, is a nickel-based solid solution-strengthened super alloy, which is widely used in applications that require high corrosion resistance. Austenite microstructure is reinforced with additional alloy elements such as Cr and Mo, which provide solid solution strengthening [8]. Duplex stainless steel (DSS) has been increasingly utilized in off-shore platforms, oil and gas, and chemical and petrochemical industries [9–12]. DSSs have continuously gained attention by their perfect strength, high toughness, and resistance to local corrosion and they have started to substitute conventional stainless steels. Service temperatures of DSSs are lower compared with Ni-based alloys because of the formation of precipitation of secondary phases such as chromium carbide, chi, sigma, and alpha-prime. These secondary phases worsen the ductility, toughness, and corrosion resistance of the alloys. One of the

---

Recommended for publication by Commission II - Arc Welding and Filler Metals

---

✉ Tuba Karahan  
tuba.karahan@gedik.edu.tr

M. Tümer  
mustafa.tumer@kocaeli.edu.tr

T. Mert  
tmert@yildiz.edu.tr

- <sup>1</sup> Kocaeli University, 41180 Kartepe/Kocaeli, Turkey  
<sup>2</sup> Yıldız Technical University, 34349 Beşiktaş/İstanbul, Turkey  
<sup>3</sup> İstanbul Gedik University, 34876 Kartal/İstanbul, Turkey

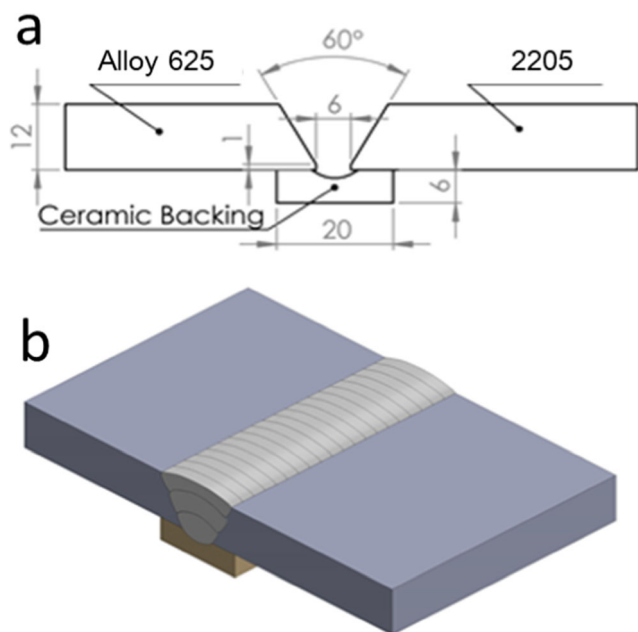


**Fig. 1** a Scheme of joint preparation, V-groove design, and ceramic backing. b Weld passes

**Table 1** Chemical composition of base and filler metals (wt%)

| Elements | Alloy 625 | 2205   | ERNiCrMo3 |
|----------|-----------|--------|-----------|
| Fe       | 4.17      | 65.800 | 1         |
| C        | 0.016     | 0.023  | 0.02      |
| Si       | 0.153     | 0.319  | 0.14      |
| Mn       | 0.162     | 1.840  | 0.2       |
| Cr       | 20.8      | 22.400 | 22        |
| Mo       | 9.05      | 3.030  | 9         |
| Ni       | 61.6      | 5.303  | 64        |
| Nb       | 3.45      | 0.008  | 3.5       |
| N        | –         | 0.166  | –         |

most important concerns in DSS is alpha-prime ( $\alpha'$ ) embrittlement. Alpha-prime embrittlement of the ferrite in 2205 DSS because of high chromium content might be an issue if the microstructure is not properly controlled [13]. On the other hand, Ni-based alloys are expensive than stainless steels [14]. Dissimilar joining between Ni-based super alloys and

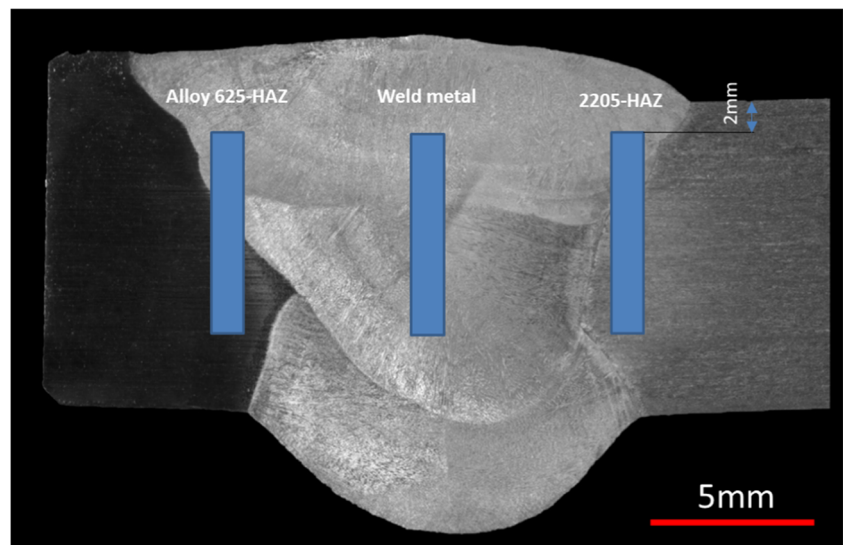
duplex stainless steels has a lot of technical advantages and offers significant cost savings in local service conditions [15, 16]. Microstructural changes and dilution occur depending on the base and filler metals, their chemical compositions, and welding conditions during joining of dissimilar metals. Intrinsically, weld metal is affected by the chemical compositions of the base metals as well as the filler metal. Joining of nickel alloys and stainless steels has been subjected to many researches in terms of the effect of the methods and the filler metals because of numerous base metal/filler metal combinations in industrial respect [15, 17–22]. Kangazian and Shamanian [23] joined SAF 2507 super duplex stainless steel and alloy 825 Ni-based super alloy, using PCGTAW and CCGTAW methods and ERNiCrMo-3 filler wire. They reported grain coarsening in alloy 825 HAZ and segregations in weld metal rich of Nb and Mo. Mortezaie and Shamanian [17] utilized GTAW in dissimilar joining of alloy 718/310S using different filler metals, i.e., ERNiCrMo3, ERNiCr3, and ER310, and in electrochemical corrosion tests of the welded samples, they obtained sorting as IN-718 BM > 310S BM > ERNiCr3 > ERNiCrMo3 > ER310 in terms of corrosion resistance. Sridhar et al. [1] joined alloy 625 and 2205 materials utilizing GTAW method and using ER2209 and ERNiCrMo-3 filler wires. Researchers reported the presence of phases rich of Nb in interdendritic zones had a detrimental effect on mechanical properties of the welded joint. In addition, they noted that weld metal toughness obtained by using ERNiCrMo-3 was higher than that of ER2209 and fracture modes of both welded samples were ductile. In another study, where the same materials were joined, Tumer et al. [24] obtained low toughness values with ER2209 duplex stainless steel filler metal. Researchers noted that the presence of Nb and Mo-rich intermetallic precipitations in the alloy 625 HAZ and root region caused a significant decrease in toughness.

The principle aim of this study is to investigate the microstructure, mechanical properties, and corrosion resistance of dissimilar joining of alloy 625 and 2205. Metal inert gas (MIG) method, which has high energy input, melting, and dilution capacity, was utilized in this study with the use of ERNiCrMo3 filler metal. The relation between toughness, microstructure, and corrosion were investigated by means of mechanical/microstructural characterization and potentiodynamic polarization tests and soundness of the joint was evaluated.

**Table 2** Process parameters employed

| Pass | Current—A | Voltage—V | Welding speed—s<br>(mm s <sup>-1</sup> ) | Heat input—Q<br>(kJ mm <sup>-1</sup> ) | Average heat<br>input—AvQ (kJ mm <sup>-1</sup> ) |
|------|-----------|-----------|--|--|--|
| 1    | 171–202   | 23.2–24.2 | 2.11                                     | 1.50–1.85                              | 1.47   |
| 2    | 207–221   | 26.0–26.8 | 2.65                                     | 1.63–1.79                              |  |
| 3    | 186–207   | 27.4–28.1 | 3.21                                     | 1.27–1.45                              |  |

**Fig. 2** Location of CVN specimens in HAZ and weld metal regions



## 2 Experimental procedure

Twelve-millimeter thick, alloy 625 and 2205 base metals were welded using MIG welding method. Ceramic backing was used below V-groove joint with  $30^\circ$  angle and 6 mm root opening (Fig. 1). Table 1 shows the chemical compositions of base and filler metals. Table 2 provides parameters in order to weld alloy 625 and 2205 dissimilar metals with a 1.2-mm ERNiCrMo3 filler wire. As a shielding gas, argon + 2% $O_2$  with a flow rate of  $20 \text{ L min}^{-1}$  was preferred. Five specimens were extracted from welded coupons after welding. Three of these were used for Charpy V-notch impact tests, one for hardness test and one for microstructural evaluation. Ground and polished surfaces were electrochemically etched with 10% oxalic acid with a potential of 10.5 V during 30 s. Olympus BX41M-LED light microscope (LM) and JEOL JSM-6060LV scanning electron microscope (SEM) with energy-dispersive spectrometry (EDS) and JEOL JEM-2100 transmission electron microscope (TEM) coupled with Oxford X-MAX 80-T EDS detector and Gatan camera were used for the characterization of the specimens. The Foundry Master Pro Optical Emission Spectrometer and the Rigaku ZSX Primus II X-Ray Spectrometer were utilized to analyze the sample cross sections in percentage weight. The impact strengths of base metal (BM), weld metal (WM), and heat-affected zone (HAZ) were identified at room temperature with V-notch impact tests and then they were compared with each other according to EN/ISO 148-1 and EN/ISO 9016 (Fig. 2). A 1000 g load (HV1) was used for micro hardness measurements with Emco DuraVision 250.

Potentiodynamic polarization tests were carried out at room temperature with potentiostat/galvanostat (PARSTAT 4000) in 3.5% wt. NaCl water solution, to evaluate the corrosion behavior of the base metal and face-root regions of the weldment. Electrochemical cell consists of conventional three-

electrode (a pair of graphite rods as the counter (auxiliary) electrodes and Ag/AgCl (3.5 mol KCl) as the reference electrode setup). The sweep potential for anodic polarization was kept within the range of  $-0.5$  to  $+0.75 \text{ V}$  at a scan rate of

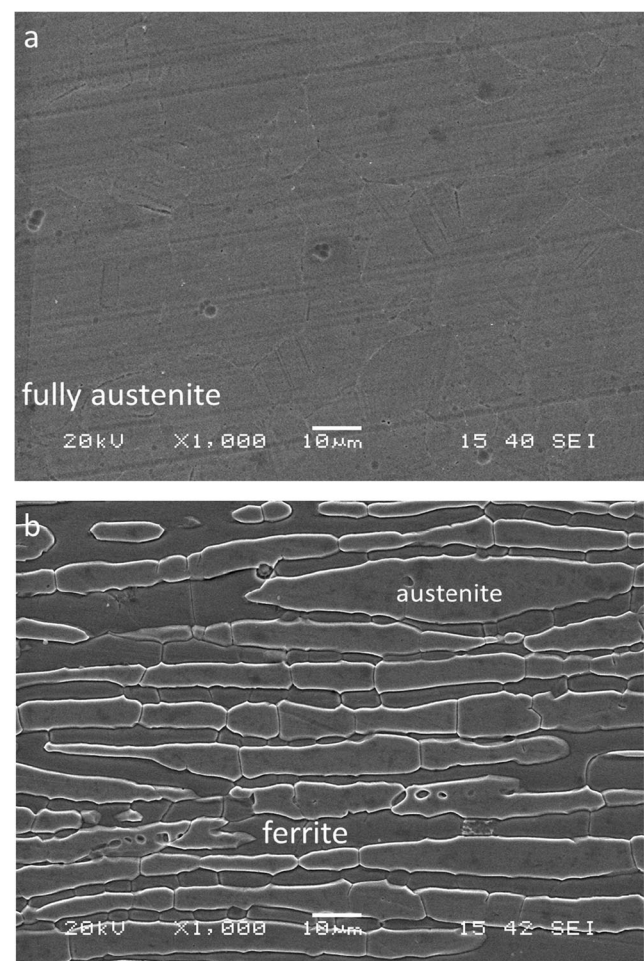


**Fig. 3** Base metal microstructure. **a** Alloy 625. **b** 2205

1 mV/s for 1800 s. According to the chemical composition of each specimen, equivalent weight calculations were accomplished by the operator of the potentiostat.

### 3 Results and discussions

#### 3.1 Microstructure

Alloy 625 is a material, which is water quenched after being subjected to annealing at 980 °C for half an hour. In Fig. 3a, equiaxed fine homogeneous  $\gamma$ -phase with carbides and

precipitates are conferred in the annealed alloy 625 and also some annealing twins were observed. Microstructure image of 2205 material is shown in Fig. 3b. When microstructure image consisting of an equal content (proportion) of ferrite and austenite phases is examined, it is clearly seen that there are austenite islets consisting of coaxial grains in the ferrite matrix, which proceed in the rolling direction. The austenite islets are generally in the form of an interconnected chain.

Figure 4 shows LM and SEM images of the microstructure of the weld metal. It is observed that the structure consists mainly of both continuous columnar and cellular dendrites (Fig. 4a). Columnar dendrites are predominant in the middle

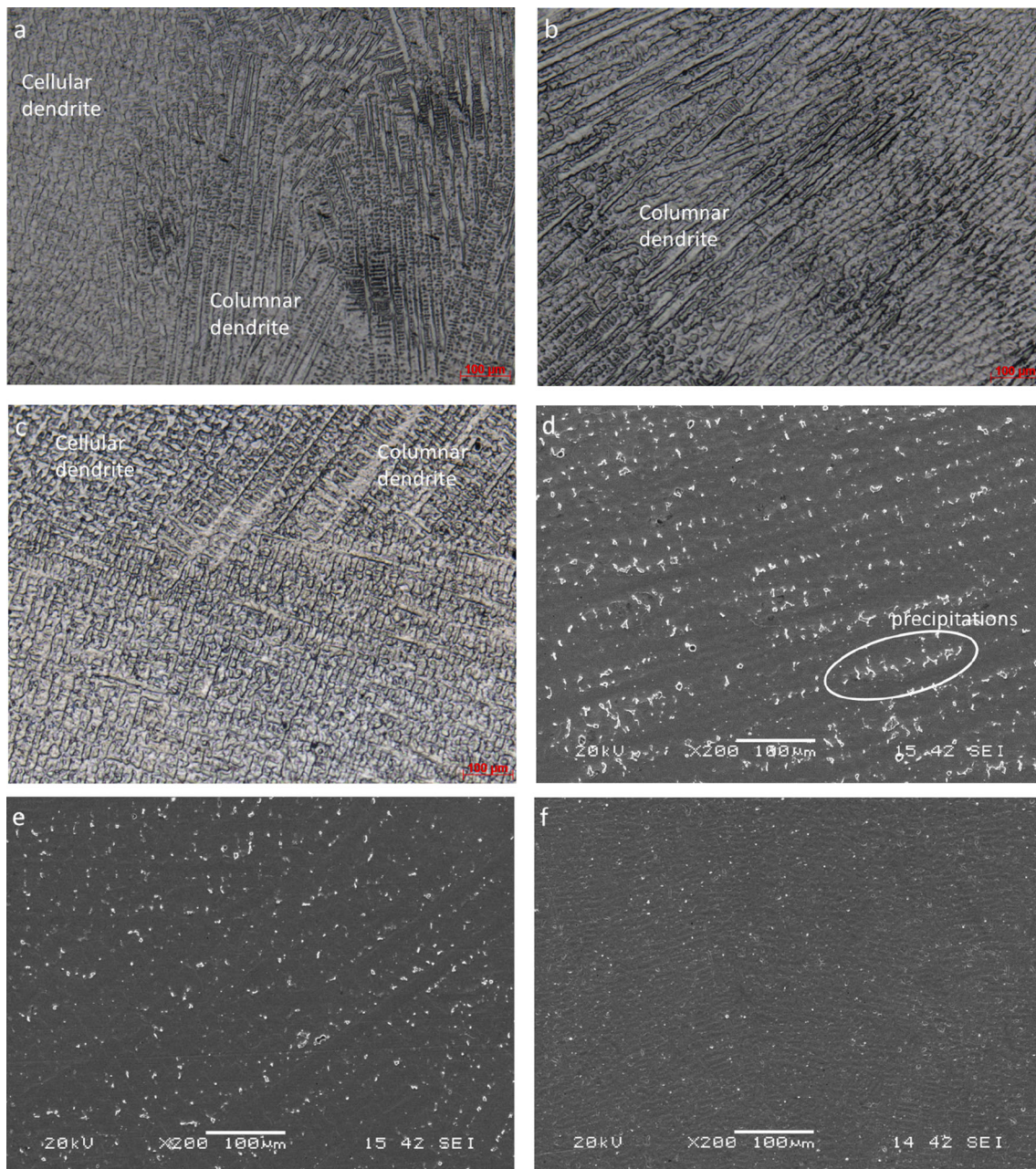
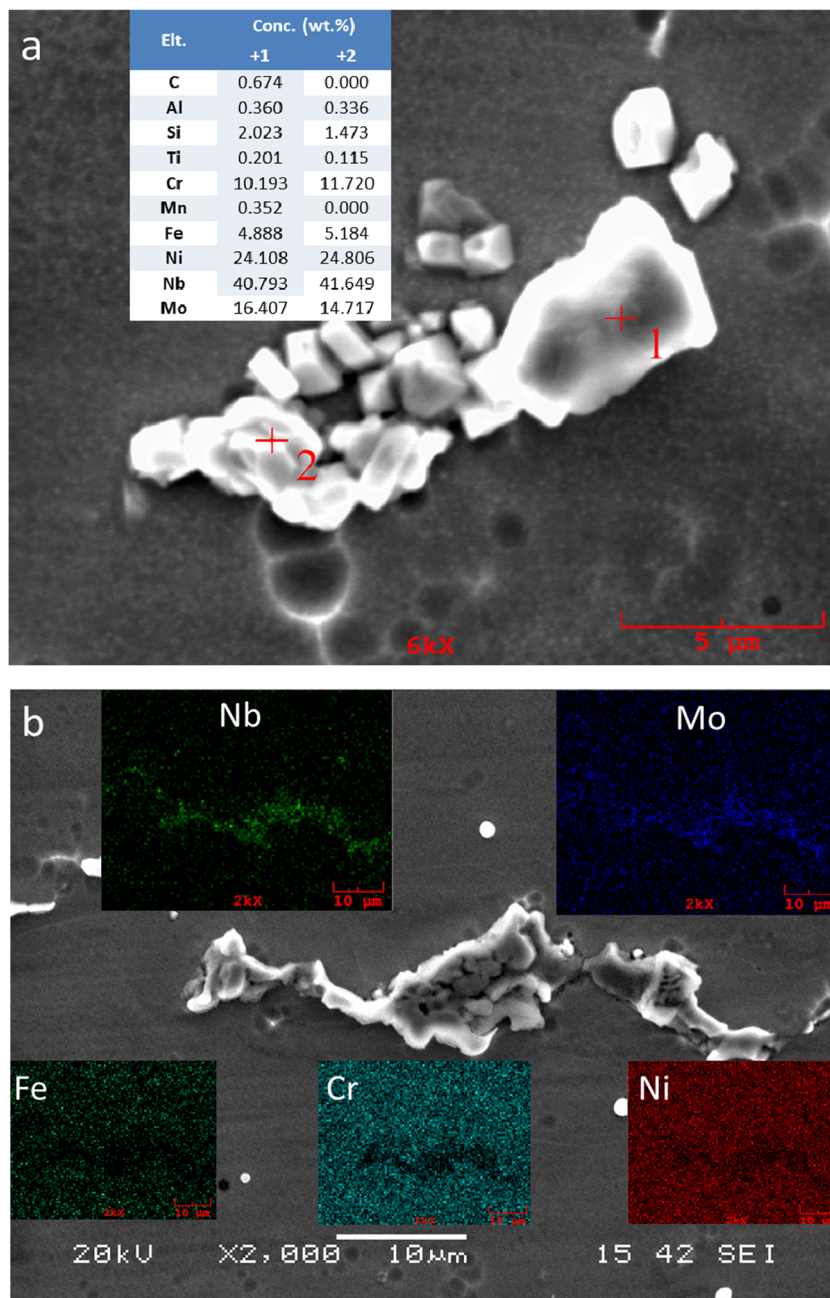


**Fig. 4** Weld metal microstructure. LM: **a** Face, **b** middle, **c** root. SEM: **d** Face, **e** middle, **f** root

pass (Fig. 4b) and columnar as well as cellular dendrites are present in root pass (Fig. 4c). When SEM image, in Fig. 4d, is examined, white precipitations are obviously seen in the entire matrix. This precipitation has an array of disjointed chains lined up between the dendrite arms. These precipitations, which are concentrated in the weld metal face area, show a significant decrease and a homogeneous distribution in the middle (Fig. 4e) and root (Fig. 4f) passes. Figure 5 presents the SEM-EDS point analyses of one precipitation from two different regions and SEM elemental mapping results of one of these precipitations in the weld metal. According to EDS analyses taken from point 1 and 2 in Fig. 5a, Nb and Mo

contents were determined as 40.793–41.649% and 16.407–14.717%, respectively. These results reveal that the formation of Nb-rich intermetallic Laves phase is common in the structure. The Laves phase is hexagonally close-packed and accepted to have  $(\text{Ni, Fe, Cr})_2(\text{Nb, Mo and Ti})$  form [21]. In NiCrMo-3-type weld metal, Laves phase forms during the last stages of solidification as part of the eutectic. It has been noted by the researchers that addition of Si and Cu in steel accelerates the precipitation of this phase [25]. In Fig. 5b, elemental mapping of the intermetallic phase taken from a different region within the weld metal is also shown. In the general form of these Nb-rich phases, Nb takes place in every region of the

**Fig. 5** SEM images from different areas in the middle of weld metal **a** point EDS analyses of spot 1 and 2. **b** Elemental mapping



intermetallic form, while the Mo element occupies a significant area in the structure, not as much as the Nb element.

LM and SEM images taken from the HAZ region are given in Fig. 6. In Fig. 6a, there are austenite grains existing perpendicular to the fusion line. The most important reason for the variation in terms of contrast in this region is the change in the chemical composition caused by dilution of Fe element on the 2205 side. Furthermore, type II grain boundary, which distinguishes itself along the fusion line, is a result of allotropic transformation in the base metal that occurs on cooling of weld metal in dissimilar welds [5, 7, 26–28] and there is needle-like (acicular) secondary nucleated austenite structure in the ferrite matrix towards 2205 base metal. There are discontinuous dendrites in columnar structure in the weld metal. The SEM image representing the same region is shown in Fig. 6b. There are intermetallic formations that occur within the columnar dendritic grains near the fusion line. Figure 6c represents alloy 625 melting zone, weld metal transition zone, and the HAZ region. There is epitaxial growth in the weld metal following the fusion line. In addition, the growth of austenite grains has occurred in an area about 200  $\mu\text{m}$  wide in the HAZ region. When the SEM image of the same region was examined in Fig. 6d, it was observed that intermetallic precipitations did not occur in the base metal and weld metal regions.

Especially, the effects of cooling rates and dilution on the duplex stainless steel side reveal an important influence on these transformations. The thermal conductivity coefficient for duplex stainless steel material is 15 W/m  $^{\circ}\text{C}$ , while it is 9.8 W/m  $^{\circ}\text{C}$  for alloy 625. Although it is assumed that low cooling rate increases the formation of Nb- and Mo-rich intermetallic phases, the dilution that ensued as a result of heat input is an important factor in formation of these phases [24, 29, 30].

Elemental mapping from the weld metal near the fusion line of 2205, where intermetallic precipitations are intense, is shown in Fig. 7. In addition to Nb- and Mo-rich intermetallics within the dendrites, the presence of elements such as Si and O from some regions has shown that oxide formations can also form structures associated with these precipitations. In general, interdendritic phases are Nb- and Mo-rich, and the morphology of these phases is related to the structure of dendrites. These phases can form an interconnected network. The fragile nature of these intermetallic phases causes poor strength, ductility, fracture toughness, fatigue, and corrosion properties of the weld metal [1].

### 3.2 Hardness

Hardness profile in face, middle, and root passes of weld metal, HAZ, and base metals is given in Fig. 8. Average hardness

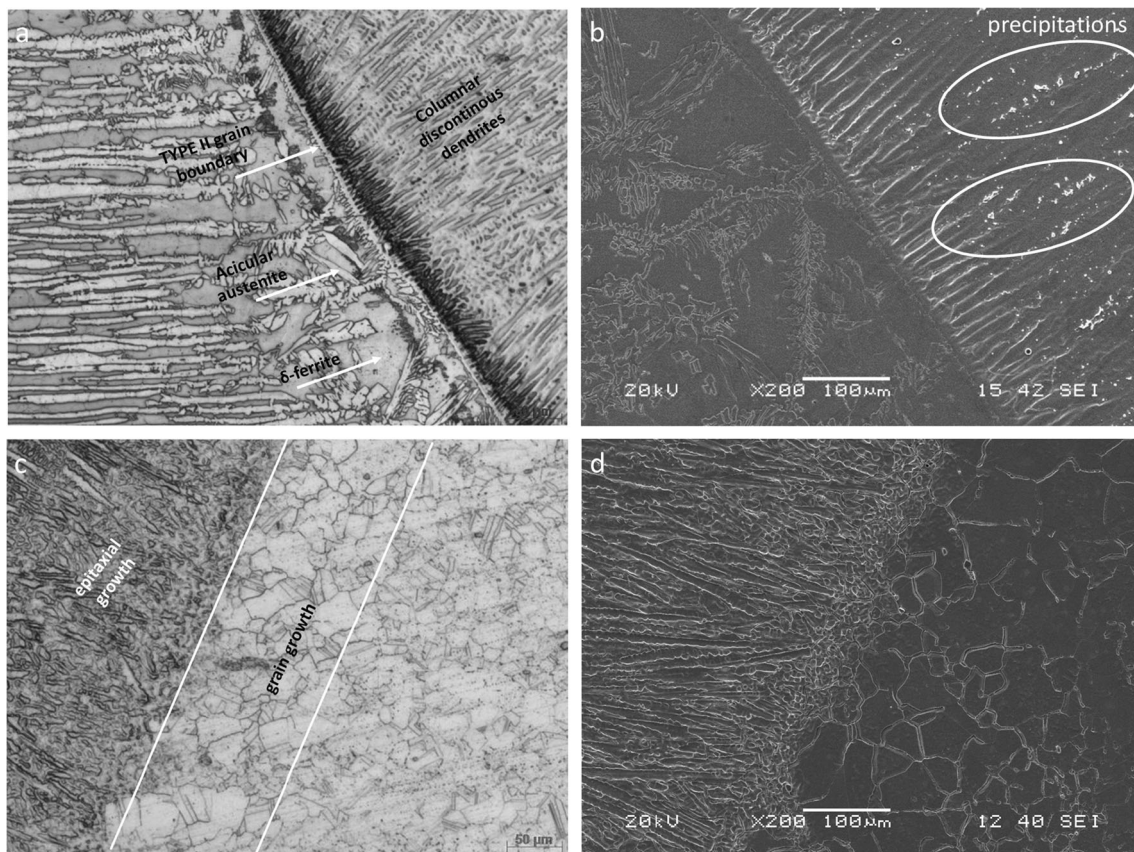


**Fig. 6** HAZ of **a** 2205 side (LM), **b** 2205 side (SEM), **c** alloy 625 side (LM), **d** alloy 625 side (SEM)

of 2205 material has been measured as  $277 \pm 9$  HV1, while it has been determined as  $283 \pm 8$  HV1 for alloy 625. Grain growth in HAZ of alloy 625 has not caused a significant decrease in hardness and it averaged  $281 \pm 5$  HV1, while it has been measured as  $272 \pm 15$  HV1 in 2205 HAZ side. The highest hardness, 290 HV1, has been achieved at the face of weld metal. Average hardness of weld metal has been observed as  $252 \pm 16$  HV1, lower than the base metals. Variations in hardness spotted in weld zone arise as a result of multi-pass welding, solidification, and different phase structures due to microstructural transformations mentioned previously. Effect of very fine intermetallic phases on hardness has not been detected.

### 3.3 Toughness and fracture surfaces

Notch impact test results for weld metal and HAZs of base metals are given in Fig. 9. Notch impact energy should be at least 47 J according to EN 14532-1. Tests applied to weld metal revealed  $103 \pm 7$  J notch impact energy. This is considered enough for a microstructure consisting of high percentage austenite phase in room temperature. Impact energies for HAZ

of alloy 625 and 2205 were  $146 \pm 10$  J and  $92 \pm 10$  J, respectively.

In Fig. 10, SEM images obtained from fracture surfaces of the tested notch impact samples at room temperature are given. Dimples, which represent ductility, are visible in high ( $\times 1000$ ) and low ( $\times 200$ ) magnifications both in weld metal and HAZs. Figure 10a and b depict fractographs of weld metal with web structure along different directions due to the cleavage of cellular dendritic grains. Fractographs of 2205 (Fig. 10c, d) and alloy 625 (Fig. 10e, f) HAZ regions showed that the fracture mainly takes place in the base metal-rich part of the weld. Dimples formed of equiaxed grains are present in both fracture surfaces. The reason why test values of 2205 HAZ are less compared with alloy 625 HAZ and weld metal zones is ferrite content in phase structure.

### 3.4 Elemental analyses

Chemical analysis results of the weld metal obtained from dissimilar joining of alloy 625–2205 materials with ERNiCrMo3 filler metal are given in Table 3. According to the elemental analysis results of weld metal, Fe element in weld metal has increased to 3.48% due to dilution from duplex

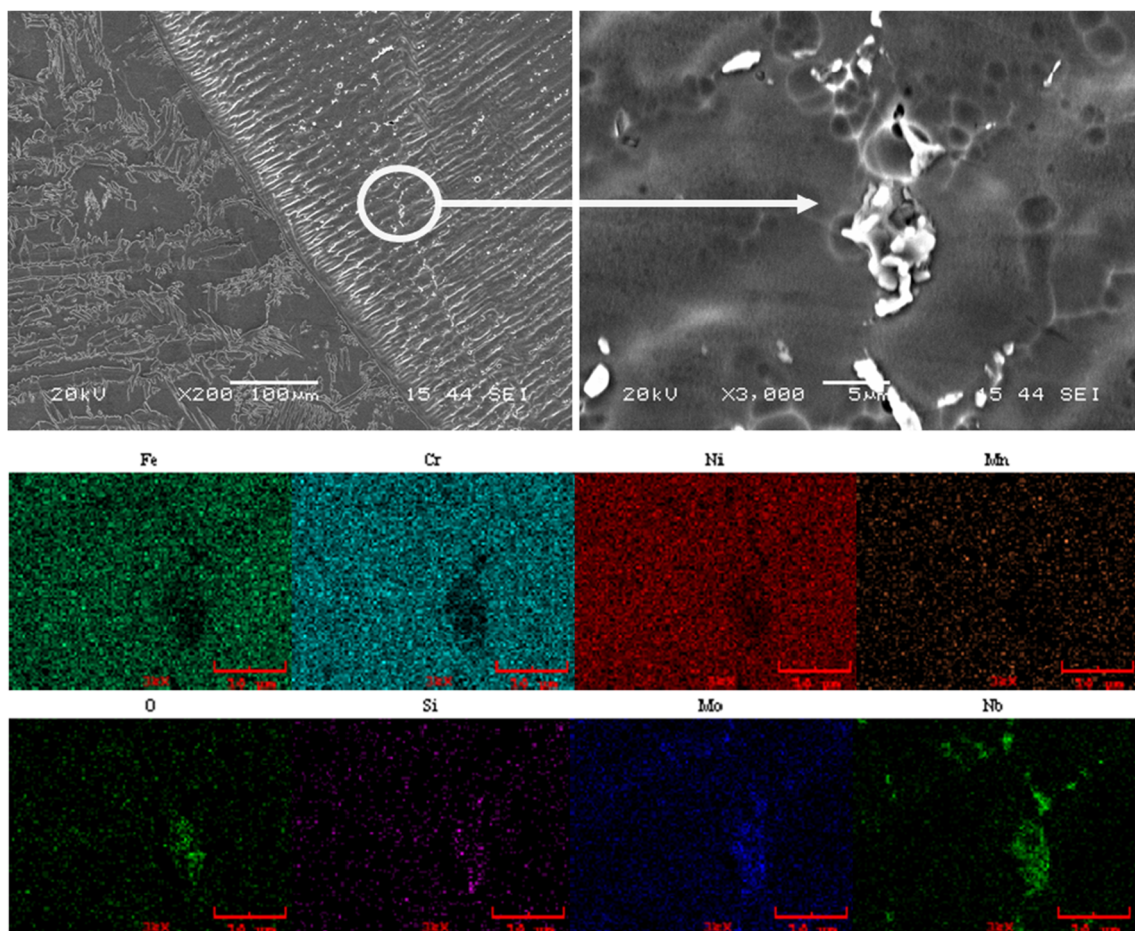
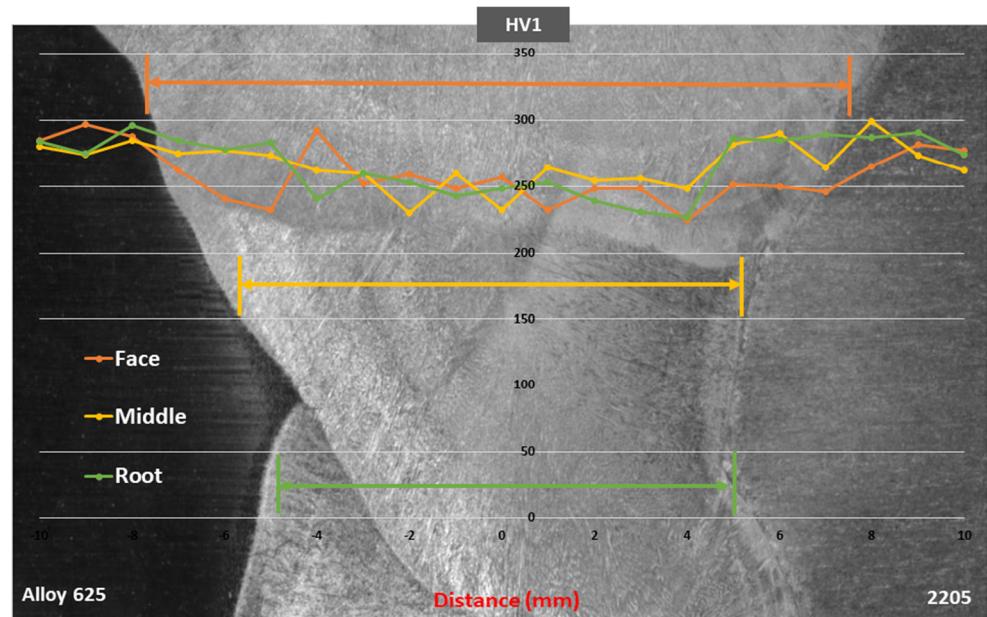


Fig. 7 SEM micrograph and elemental mapping of intermetallic precipitation at fusion line of 2205

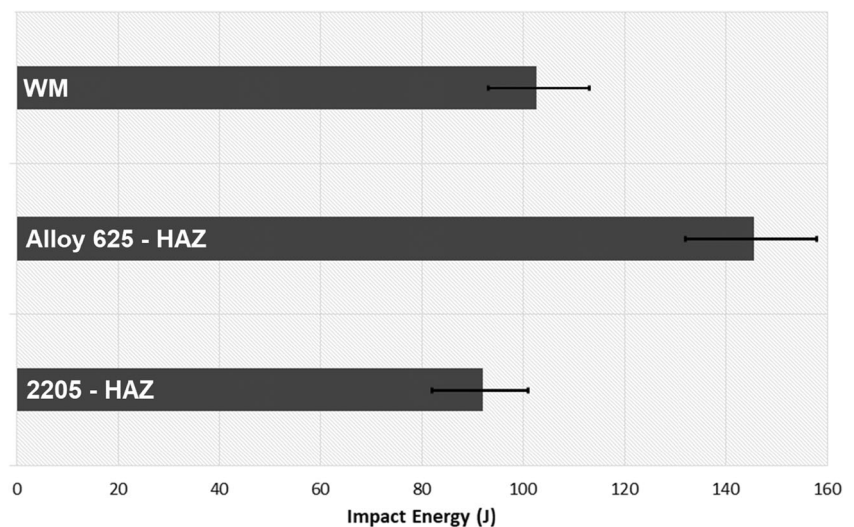
**Fig. 8** Hardness profile of face, middle, and root passes of weld metal, HAZ, and base metals



stainless steel material, although this element's weight percentage was 1 in filler metal. Elemental migration due to dilution was not significant for other elements except for Fe. In addition to average OES results obtained from face, middle, and root zones, elemental mapping (Fig. 11) in an area with 4 mm width between face and root passes has been realized in order to observe elemental variations of Fe, Ni, Cr, Mo, and Nb, which play an important role in microstructure of weld metal, between passes.

The lowest value of Fe observed is 3%, while the highest is above 10%. Melting of 2205 material at the root caused a significant Fe element migration in the weld metal. Moreover, the increase of Fe element at the root region led to decrease of the content of Nb and Mo elements that formed intermetallic phases. This case, especially, is the reason for less formation of intermetallic phase formations at the root region.

**Fig. 9** Impact energies of weld metal, alloy 625 HAZ, and 2205 HAZ



### 3.5 TEM analysis

TEM analysis obtained from the weld metal is given in Fig. 12. Figure 12a and b depict bright field (BF) images of lump-like precipitations in matrix. Selected area diffraction (SAD) pattern is given in Fig. 12c. These lump-like precipitations observed in weld metal microstructure have been defined as Laves phase, which has hexagonal close-packed crystal structure formed by secondary heat input [31]. Diffraction model obtained presents nanosized oxide particulates, which have spinel structure in outer layer. Morphologies of the Nb-enriched interdendritic Laves phases are related to dendritic structure and they can form an interconnected network [32].



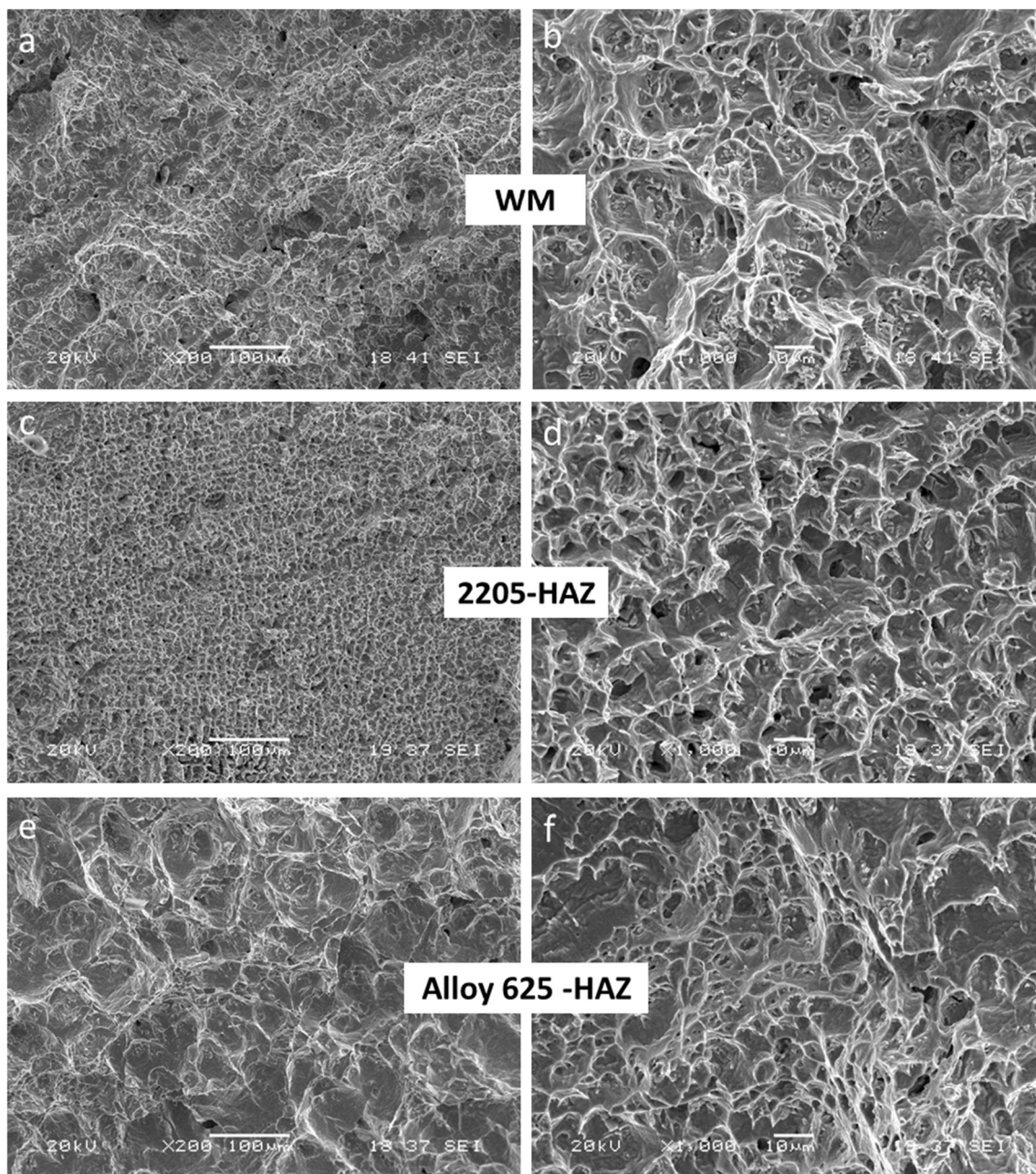


**Fig. 10** SEM images of fracture surfaces of WM, 2205 HAZ, alloy 625 HAZ (left  $\times 200$ , right  $\times 1000$ )

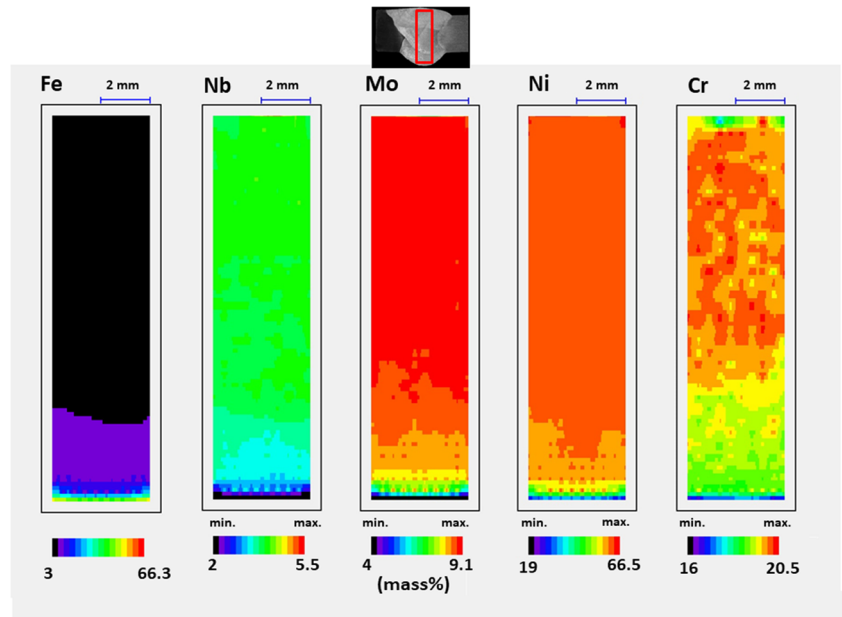
**Table 3** Weld metal chemical analysis

| Elements | wt%   |
|----------|-------|
| Fe       | 3.48  |
| C        | 0.009 |
| Si       | 0.172 |
| Mn       | 0.183 |
| Cr       | 21.4  |
| Mo       | 9.13  |
| Ni       | 61.8  |
| Nb       | 3.5   |

### 3.6 Corrosion

Figure 13 presents the results of potentiodynamic polarization tests applied to base materials, weld metal face, and root areas, and also Table 4 informs their relevant data from electrochemical measurements. Corrosion potential is the static indicator of electrochemical corrosion resistance which reveals corrosion sensitivity [2]. Generally, materials that exhibit high corrosion potential provide higher corrosion resistance. Corrosion current density is related to corrosion kinetics, which emerge in the material. Corrosion current density indicates the current flowing from a corroded unit surface. When

**Fig. 11** Elemental mapping of weld metal



this value gets higher, the corrosion rate and damage inside the material increase. Thus, corrosion current density has a direct effect on corrosion rate. It was stated all the samples actively dissolved when the polarization curves were studied. When the results are evaluated in terms of the corrosion potential,

this sorting is gathered: WM-root > 2205 > Alloy 625 > WM-face. WM-face is the most sensitive-to-corrosion zone of the joint. Contrary to this, weld metal root is the most corrosion-resistant zone. The most important cause for this case is the intermetallic phase formation in weld face compared with the

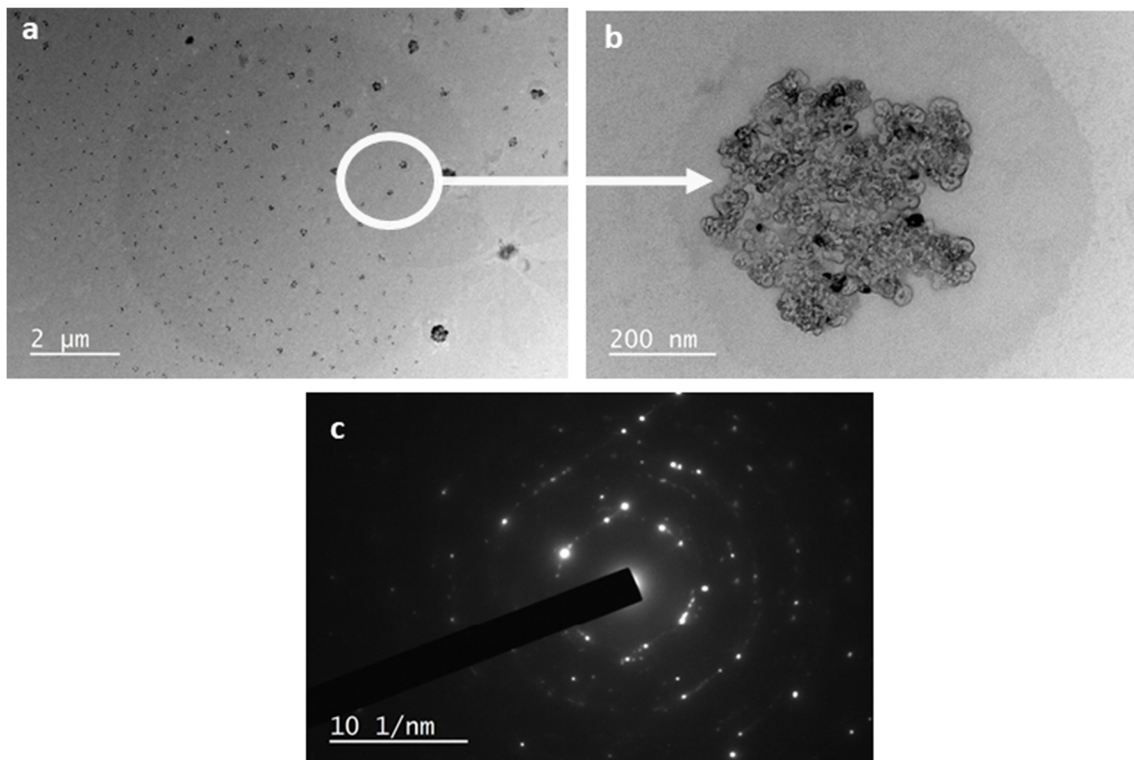


**Fig. 12** TEM images obtained from the weld metal **a** bright field (BF) image of precipitation phase. **b** High magnification BF image of precipitation. **c** Selected area diffraction (SAD) pattern

**Table 4** Electrochemical parameters of BMs and WM-root/face

| Specimen  | Surface area (cm <sup>2</sup> ) | Density (g/cm <sup>3</sup> ) | Equivalent weight (kg/mol) | Corrosion current (μA) | Corrosion current density I <sub>corr</sub> (μA/cm <sup>2</sup> ) | Corrosion rate (mm/year) | Corrosion potential E <sub>corr</sub> (mV) |
|-----------|---------------------------------|------------------------------|----------------------------|------------------------|---|--------------------------|--|
| Alloy 625 | 0.283                           | 8.25                         | 27.25                      | 0.195                  | 0.689   | 0.007                    | −131.7                                     |
| WM-root   | 0.283                           | 8.30                         | 27.75                      | 0.207                  | 0.731   | 0.008                    | −96.2                                      |
| WM-face   | 0.283                           | 8.30                         | 27.75                      | 0.334                  | 1.180   | 0.013                    | −165.4                                     |
| 2205      | 0.283                           | 7.80                         | 19.79                      | 0.239                  | 0.844   | 0.007                    | −98.5                                      |

middle of the weld and the root. Intermetallic phases emerged in these zones are effective on corrosion current density and corrosion rates. The presence of these phases raised these two factors. Intermetallic phases affect in decrease of corrosion resistance and increase in corrosion rate. Micro galvanic cells form inside the material in the presence of intermetallic phase and tendency to dissolution increases with the formation of anode-cathode zones [17].

#### 4 Conclusion

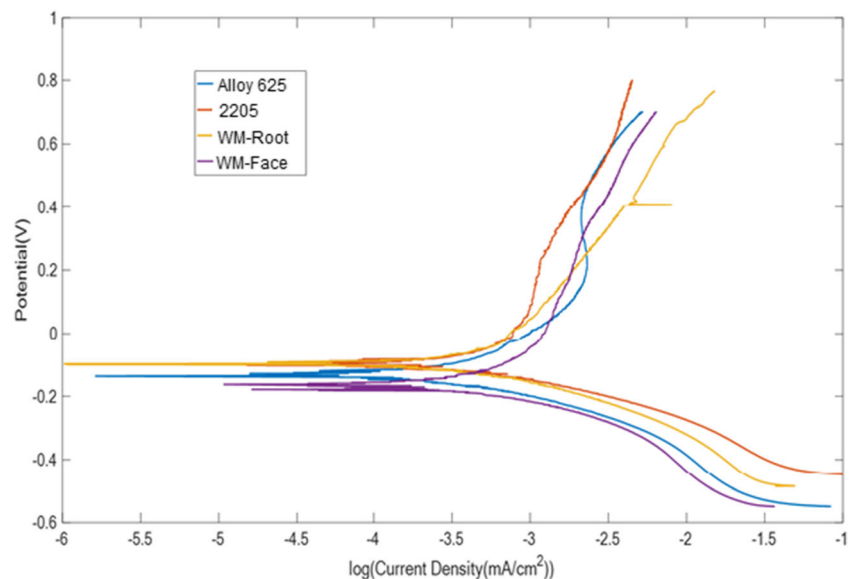
The mechanical properties of the joint of MIG-welded alloy 625 with 2205 using ERNiCrMo-3 filler metal were sufficient. Relationship in terms of mechanical and microstructural properties of the welded joints, and the causes of the problems encountered in the weld metal were scrutinized and the results are listed below.

- (1) In consequence of the dilution from 2205 side, the percentage of Fe element in the weld metal has increased. Especially, increasing Fe dilution in the root region decreased the rate of the other elements. Although iron

promotes the Laves phase, Nb and Mo elements affect more in this respect [7]. In elemental mapping of weld metal (Fig. 11), it is depicted that iron is a bit higher in root compared with face region because of the dilution from 2205. On the contrary, Nb and Mo, which are predominant elements in the formation of Laves phase, are less in the root region compared with face region. In addition, interdiffusion of elements and dissolution caused by tempering effect of middle and face passes have yielded less Laves phase formation in the root.

- (2) Microstructures of Nb- and Mo-rich intermetallic Laves phases are located in dendrite or cellular structure. Although there is a more intense formation in the middle and face passes, the formation in the root zone is less. While this phase almost never occurred in the weld metal close to the alloy 625 HAZ region, it is distinguished among the dendrite arms in the weld metal close to the fusion line of the 2205.
- (3) The notch impact tests of the weld metal and HAZs of both base materials revealed that the joint had sufficient impact toughness. Intermetallic phases and inclusions prevent the impact toughness of the joint to be as high as the base material.

**Fig. 13** Potentiodynamic polarization curves



**Acknowledgements** The authors would like to acknowledge the welding consumable support from Gedik Welding.

## References

- Sridhar R, Devendranath Ramkumar K, Arivazhagan N (2014) Characterization of microstructure, strength, and toughness of dissimilar weldments of Inconel 625 and duplex stainless steel SAF 2205. *Acta Metall Sin (English Lett)* 27:1018–1030. <https://doi.org/10.1007/s40195-014-0116-5>
- Wang S, Ma Q, Li Y (2011) Characterization of microstructure, mechanical properties and corrosion resistance of dissimilar welded joint between 2205 duplex stainless steel and 16MnR. *Mater Des* 32:831–837. <https://doi.org/10.1016/j.matdes.2010.07.012>
- Jang C, Lee J, Sung Kim J, Eun Jin T (2008) Mechanical property variation within Inconel 82/182 dissimilar metal weld between low alloy steel and 316 stainless steel. *Int J Press Vessel Pip* 85:635–646. <https://doi.org/10.1016/j.ijpvp.2007.08.004>
- Benhadad S, Richards NL, Chaturvedi MC (2002) The influence of minor elements on the weldability of an INCONEL 718-type superalloy. *Metall Mater Trans A Phys Metall Mater Sci* 33:2005–2017. <https://doi.org/10.1007/s11661-002-0033-5>
- Dehmlaei R, Shamanian M, Kermanpur A (2008) Microstructural characterization of dissimilar welds between alloy 800 and HP heat-resistant steel. *Mater Charact* 59:1447–1454. <https://doi.org/10.1016/j.matchar.2008.01.013>
- Ramkumar KD, Kumar PSG, Radhakrishna VS et al (2015) Studies on microstructure and mechanical properties of keyhole mode Nd: YAG laser welded Inconel 625 and duplex stainless steel, SAF 2205. *J Mater Res* 30:3288–3298. <https://doi.org/10.1557/jmr.2015.276>
- DuPont NJ, Lippold CJ, Kiser DS (2009) Welding metallurgy and weldability of nickel based alloys. John Wiley & Sons Inc, Hoboken
- Xing X, Di X, Wang B (2014) The effect of post-weld heat treatment temperature on the microstructure of Inconel 625 deposited metal. *J Alloys Compd* 593:110–116. <https://doi.org/10.1016/j.jallcom.2013.12.224>
- Zhang Z, Jing H, Xu L, Han Y, Zhao L (2016) Investigation on microstructure evolution and properties of duplex stainless steel joint multi-pass welded by using different methods. *JMADE* 109: 670–685. <https://doi.org/10.1016/j.matdes.2016.07.110>
- Tavares SSM, Pardal JM, Lima LD, Bastos IN (2007) Characterization of microstructure, chemical composition, corrosion resistance and toughness of a multipass weld joint of superduplex stainless steel UNS S32750. *58:610–616*. <https://doi.org/10.1016/j.matchar.2006.07.006>
- Moteshakker A, Danaee I (2016) Microstructure and corrosion resistance of dissimilar weld-joints between duplex stainless steel 2205 and austenitic stainless steel 316L. *J Mater Sci Technol* 32: 282–290. <https://doi.org/10.1016/j.jmst.2015.11.021>
- Westin EM, Sieurin H, Sandstro R (2006) Fracture toughness of the lean duplex stainless steel LDX 2101. *Metall Mater Trans A* 37: 2975–2981
- Lippold JC, Kotecki DJ (2005) Welding metallurgy and weldability of stainless steels. John Wiley & Sons Inc, Hoboken
- Kangazian J, Shamanian M, Ashrafi A (2017) Dissimilar welding between SAF 2507 stainless steel and Incoloy 825 Ni-based alloy: the role of microstructure on corrosion behavior of the weld metals. *J Manuf Process* 29:376–388. <https://doi.org/10.1016/j.jmapro.2017.08.012>
- Sireesha M, Albert SK, Shankar V, Sundaresan S (2000) A comparative evaluation of welding consumables for dissimilar welds between 310 austenitic stainless steel and Inconel 657. *J Nucl Mater* 279:65–76
- Shama S, Taiwade RV, Vashishtha H (2017) Effect of pulsed current gas tungsten arc process on the dissimilar weldments between nickel-based superalloy/ austenitic stainless steel. *J Mater Eng Perform* 26: 1146–1157. <https://doi.org/10.1007/s11665-017-2570-5>
- Mortezaie A, Shamanian M (2014) An assessment of microstructure, mechanical properties and corrosion resistance of dissimilar welds between Inconel 718 and 310S austenitic stainless steel. *Int J Press Vessel Pip* 116:37–46. <https://doi.org/10.1016/j.ijpvp.2014.01.002>
- Naffakh H, Shamanian M, Ashrafzadeh F (2009) Dissimilar welding of AISI 310 austenitic stainless steel to nickel-based alloy Inconel 657. *J Mater Process Technol* 209:3628–3639. <https://doi.org/10.1016/j.jmatprotec.2008.08.019>
- Hosseini HS, Shamanian M, Kermanpur A (2016) Microstructural and weldability analysis of Inconel617/AISI 310 stainless steel dissimilar welds. *Int J Press Vessel Pip* 144:18–24
- Li G, Huang J, Wu Y (2014) An investigation on microstructure and properties of dissimilar welded Inconel 625 and SUS 304 using high-power CO2 laser. *Int J Adv Manuf Technol* 76:1203–1214. <https://doi.org/10.1007/s00170-014-6349-7>
- Hejripour F, Aidun DK (2017) Consumable selection for arc welding between stainless steel 410 and Inconel 718. *J Mater Process Technol* 245:287–299
- Kumar KG, Ramkumar KD, Arivazhagan N (2015) Characterization of metallurgical and mechanical properties on the multi-pass welding of Inconel 625 and AISI 316L. *J Mech Sci Technol* 29:1039–1047. <https://doi.org/10.1007/s12206-014-1112-4>
- Kangazian J, Shamanian M (2018) Characterization of structure–property relationship of Incoloy 825 and SAF 2507 dissimilar welds. *Trans Indian Inst Metals* 71:1747–1757. <https://doi.org/10.1007/s12666-018-1309-9>
- Tumer M, Karahan T, Mert T (2020) Evaluation of microstructural and mechanical properties of dissimilar Inconel 625 nickel alloy–UNS S32205 duplex stainless steel weldment using MIG welding. *Weld World* 64:21–35. <https://doi.org/10.1007/s40194-019-00825-x>
- Korcakova L (2002) Microstructure evolution in high strength steel for power plant application - microscopy and modelling
- Sireesha M, Shankar V, Albert SK, Sundaresan S (2000) Microstructural features of dissimilar welds between 316LN austenitic stainless steel and alloy 800. *Mater Sci Eng A* 292:74–82. [https://doi.org/10.1016/S0921-5093\(00\)00969-2](https://doi.org/10.1016/S0921-5093(00)00969-2)
- Ranjbar K, Dehmlaei R, Amra M, Keivanrad I (2018) Microstructure and properties of a dissimilar weld between alloy 617 and A387 steel using different filler metals. *Weld World* 62: 1121–1136. <https://doi.org/10.1007/s40194-018-0610-x>
- Gunn R (1997) Duplex stainless steels: microstructure, Properties and Applications. Abingt Publ
- Ramkumar KD, Kumar BM, Krishnan MG, Dev S, Bhalodi AJ, Arivazhagan N, Narayanan S (2015) Studies on the weldability, microstructure and mechanical properties of activated flux TIG weldments of Inconel 718. *Mater Sci Eng A* 639:234–244. <https://doi.org/10.1016/j.msea.2015.05.004>
- Manikandan SGK, Sivakumar D, Rao KP, Kamaraj M (2014) Effect of weld cooling rate on Laves phase formation in Inconel 718 fusion zone. *J Mater Process Technol* 214:358–364. <https://doi.org/10.1016/j.jmatprotec.2013.09.006>
- Wang W, Cao X, Lu Y, Ding X, Shoji T (2017) TEM study on oxide mechanism of the dissimilar welds between 316 stainless steels/Inconel 182 in high temperature and high pressure water. *Mater Charact* 131: 339–347. <https://doi.org/10.1016/j.matchar.2017.07.004>
- Xu F, Lv Y, Liu Y, Shu F, He P, Xu B (2013) Microstructural evolution and mechanical properties of Inconel 625 alloy during pulsed plasma arc deposition process. *J Mater Sci Technol* 29: 480–488. <https://doi.org/10.1016/j.jmst.2013.02.010>

**Publisher's note** Springer Nature remains neutral with regard to jurisdictional claims in published maps and institutional affiliations.